Clustering Artificial Atoms Induced by High-Frequency Electromagnetic Radiation in Graphene Monolayers of Multiwalled Carbon Nanotubes

H. V. Grushevskaya,* A. I. Timoshchenko,† E. A. Avdanina, and I. V. Lipnevich
Physics Department, Belarusian State University,
4 Nezalezhnasti Ave., 220030 Minsk, BELARUS
(Received 26 September, 2020)

A graphene-charge carrier confinement induced by high-frequency photons and a subsequent clustering of artificial atoms in graphene plane have been studied using electrophysical and Raman-spectroscopy methods. To fabricate the graphene n-p-n junctions, commensurable superlattice structures consisting of multi-walled carbon nanotubes (MWCNTs) have been formed utilizing a Langmuir-Blodgett technique. It has been shown that the p-n graphene junctions are sensitive to graphene lattice-deformation defects only. The levels of graphene defect do not host impurity electrons. One offers a mechanism of graphene monolayer self-repairing after a radiation damage. This mechanism is based on an existence of topologically protected Compton scatterers in graphene plane.

1. Introduction

Graphene, carbon nanotubes (CNT), and graphene-like materials can exhibit radiation resistance and are promising structural materials for nuclear applications, for example, new generation of photodetectors [1] and as a replacement for plastic beta-scintillators [2] due to the following features. Band structure of graphene materials is gapless, their bands are touched, and chiral charge carriers are massless. Lindhard atom screening [3] happens in graphene and ultrathin crystal so that noninteracting with electrons incoming particles are scattered by a crystal-plane atom potential. Subsequently a fast surface diffusion of knocked-out C atoms proceeds very fast in the vacancies places (vacancy annealing) [4]. The atoms, which are knocked out of the graphene plane or ultrathin crystal under action of high-energy (1 MeV–1 GeV) ions [5–7],

electrons (see [6, 8–10] and references therein), protons and positrons (see [6, 11] and references therein), cannot escape from the graphene plane to enter the deep bulk region. Emerging in beta-rays-,ions-irradiated graphene the radiation vacancies form clusters. [8, 12, 13] The vacancies are neutral, but they host a positively charge by applying electromagnetic pulses [13].

As well, radiation resistivity of MWCNTs is revealed as a possibility for carbon atoms to be displaced by gamma-rays in the vicinity of graphene plane only that a radiation structural rearrangement is restricted to chemical cross link of the nearest carbon nanotubes by formation of chemical bonds between neighbor C atoms from graphene layers or between C atoms on the interface CNT–environment [7, 12]. However, the relation between the ability of vacancies to cluster formation and the ability of multiwalled CNTs (MWCNTs) to self repair is not clearly understood.

Chiral massless charge carriers in graphene form electron-hole pairs. An electron-hole density in the Dirac point $K(K')$ of graphene Brillouin

————
*E-mail: `grushevskaja@bsu.by`
†E-mail: `a_timoshchenko@mail.ru`

zone is extremely high due to the fact that the energy of electron-hole pair is zero. The value of hole/electron density is high enough to provide trapping of bombarding negatively/positively electrically charged particle. The last will also be impeded to channeling of 1 MeV–1 GeV electrons and consequently to a generation of X- and γ-rays, stimulated by the curvature of CNTs or similar periodically-bent crystalline structures. The presented mechanism of trapping is also in agreement with the absence of experimental facts about such type of generation [14] theoretically predicted in [15, 16]. Because of the gapless structure, the interaction between graphene and electro-magnetic radiation presents itself an elastic scattering of gamma-quanta on free charge carriers. Notwithstanding large Compton effect, an ultrafast hot carrier recombination on a sub-picosecond timescale attenuates sharply the response of modern graphene broadband photodetectors [17].

So, the most fundamental radiation damage studies, such as many-body surface-defect evolution processes, are lacking.

In the paper we study the influence of weak flows of gamma- and beta-ray particles from radiation source of ^{137}Cs on electrophysical properties of ultra-thin Langmuir–Blodgett (LB) films which have been fabricated from MWCNTs decorated by organometallic compound. We demonstrate that the electrophysical properties of LB-films are recovered after irradiation. Moreover, shielding effect of the high-conductivity MWCNT LB-bundles is sharply enhanced. To discover a mechanism of graphene radiation resistance we will also utilize laser pulses to produce the n-p-n junctions of p-doped and n-doped patches in graphene-like materials of different types. The junctions induced by the hight-frequency electromagnetic radiation will be investigated by Raman spectroscopy methods.

2. Methods

2.1. Sample fabrication

Carboxylated and stearic-acid-functionated MWCNTs under 2.5–5 nm in diameter have been decorated by nanocyclic complexes (Fe(II)DTP) of Ce and/or high-spin octahedral Fe with ligands being conducting oligomer of dithionylpyrrole series in the following way. As a preliminary, an alkyl hydrocarbon chain $C_{16}H_{33}$ was linked chemically to the oligomer. Chemical formula of the oligomer has the following form: 3-hexadecyl-2,5-di(thiophen-2-yl)-1H-pyrrole (H-DTP). A 5-monolayer graphene-like film of the nanocyclic organometallic complexes is fabricated by means of LB-nanotechnique. Then, inverse micelles of stearic acid with MWCNTs inside are obtained by mixing stearic acid and MWCNTs in hexane by the ultrasound treatment, and 2-monolayer MWCNT films fabricated from these micellar MWCNTs by LB-nanotechnique are deposited on the nanocyclic-complex LB-cover. The MWCNT LB-bundles nondecorated/decorated by organometallic complexes or the LB-films of nanocyclic organometallic complexes were deposited on the interdigital structure of aluminium electrodes, on the surface of which a layer of nanoporous anodic alumina (AOA) were previously formed as a insulator coating.

2.2. Supports modifications

Hydrophilization of Si surface was performed by its treating with mixture of sulphuric acid (H_2SO_4) and hydrogen peroxide (H_2O_2) for 30 min. It ordinary is used to remove organic residues from a substrate. After that, the Si plate was washed out in deionized water followed by the ultrasound treatment for 10 min. Meanwhile, additionally to the organic substrates were removed from the Si surface, a hydrophilic film of SiO_2 is formed with very flat surface [18] The surface of nanoporous anodic alumina is hydrophilic. For its hydrophobization the solution of H-DTP in hexane was dropped on the surface.

2.3.   Exposure to radiation

A low-intensive source of ionizing radiation (IRS) ^{137}Cs (CsJ) with activity of radioactive decay A about 6.22×10^4 Bq at the time of investigation. Beta-decay of unstable nuclei ^{137}Cs is accompanied by emission of beta-particles with the energies 0.512, 0.892, and 1.176 MeV and by production of Ba nuclei. 94.7% of Ba nuclei being in metastable state emit gamma-quanta with mean energy 662 keV [19]. The radiation of low-intensive beta-particles beam has been attenuated by thin-film aluminium screen. The irradiation dose was chosen to be 10^{-9} Gy/hour. The IRS has the form of a drop with average diameter about $d = 1.5$ mm. A sample with diameter $D_s = 4$ mm is exposed through collimator being of the order of 5 mm in diameter and $L = 50$ mm long. A scheme of irradiation is shown in fig. 1. At ratio $d/L = 0.03$, IRS can be considered as a point source.

A scintillation detector has been constructed based on NaJ(Te) crystal having diameter of 25 mm and hight of 40 mm. A fluence rate of nonscattered gamma-radiation within the irradiated sample can be estimated as

$$\phi_0 = \frac{kA}{4L^2} \frac{\pi D_s^2}{4L^2} \qquad (2.1)$$

where k is a percentage of emitted photons per one decay (so called quantum yield), $\frac{\pi D_s^2}{4L^2}$ is a solid angle under which the irradiated sample is viewed from the point of IRS. For IRS ^{137}Cs $k = 0.851$. Therefore $\phi_0 = 8.5 \times 10^3$ m^{-2}c^{-1}. A number of γ-quanta coincides with a number of 0.512 MeV electrons emitted by ^{137}Cs atoms in decay process. Since the percentage of 1.174 MeV electrons is 5.3 %, the fluence of beta-quanta with the energy 1.174 MeV is less than 485 m^{-2}c^{-1}. Irradiation of the organometallic LB-films has been performed for 1 hour, MWCNTs were exposed to radiation for 1 or 3 hours. A graphene monolayer deposited on the insulator surface which becomes electric under the action of β-radiation [32] is doped. To avoid parasitic doping, the graphene materials suspended on nanoporous AOA were irradiated only.
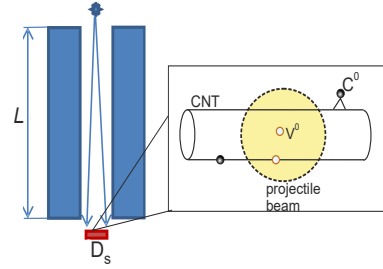

FIG. 1. (color online) A scheme of irradiation of sample (underneath the collimator of length L) of diameter D_s. IRS is placed above the collimator. Inset : Sketch of radiation defects presents creation of neutral vacancies V^0 with knocked-out neutral atoms C^0 fixed on nanotube wall (graphene monolayer).

Samples are exposed to laser radiation at light wavelengths 355, 473, and 532 nm with power in range from 0.0001 to 20 mW at room temperatures (RT).

2.4.   Impedance measurements

We use the planar capacitive sensor of interdigital-type on such glass-ceramic support as pyroceramics [20]. N pairs, $N = 20$ of aluminium electrodes of the sensors are arranged in an Archimedes-type spiral configuration. Every such pair is an "open type" capacitor. The dielectric coating of the electrodes represents itself nanoporous anodic alumina with a pore diameter of 10 nm. The synthesized LB-nanoheterostructures were suspended on the interdigital electrode structure. To excite harmonic auto-oscillations of electric current (charge–discharge (charging) processes in the capacitors), the sensor was connected as the capacitance C into the relaxation resistance (R)–capacitance (C) oscillator (self-excited RC-oscillator) [21]. Operating of such RC- oscillator is based on the principle of self-excitation of an amplifier with a positive feedback on quasi-resonance frequencies. The capacitance C of the sensor entered in measuring RC-oscillating circuit has been calculated by the formula $C = 1/(2\pi R f)$, where R is the measuring

resistance, f is a quasi-resonance frequency. Electrophysical properties of the ultra-thin LB-films were studied by means of the impedance spectroscopy methods as a variation in dielectric polarization of double electrically charged layer formed at the interface between a surface of the fabricated electrochemical sensor and water. Electrochemical measurements were carried out in deionized water at RT.

2.5. Raman spectroscopy studies

Spectral studies in visible range were carried out using a confocal micro-Raman spectrometer Nanofinder HE ("LOTIS-TII", Tokyo, Japan–Belarus).

2.6. Theoretical modeling

A quasi-relativistic graphene model Hamiltonian reads [22–25]

$$v_F \left[\vec{\sigma}_{2D}^{AB} \cdot \vec{p}_{BA} - c^{-1} M_{BA} \right] |\psi_{BA}^*\rangle = E |\psi_{BA}^*\rangle \quad (2.2)$$

and the same equation with labels (AB, BA) exchanged for another sublattice. Here

(AB, BA) are related to sublattices and refer to the quantities which are obtained by similar transformations with a relativistic exchange matrix Σ_{rel}^x e.g., for the momentum operator $\vec{p}$ one gets $\vec{p}_{BA} = \Sigma_{BA} \, \vec{p} \, \Sigma_{BA}^{-1}$; v_F is the Fermi velocity. The vector of 2D Pauli matrixes comprises of two matrixes $\sigma_{2D} = (\sigma_x, \sigma_y)$. The term $M_{BA} = -\frac{1}{cv_F}\Sigma_{BA}\Sigma_{AB}$ is a Majorana-like mass term, where c is the speed of light. It turns out to be zero in the Dirac point $K(K')$ and gives a very small momentum-dependent correction outside of $K(K')$. The relativistic exchange operator for tight-binding approximation and accounting of nearest lattice neighbors is given by its action on secondary quantized wave functions on trigonal sublattices $A(B)$ of the system as [22, 24, 25]

$$\Sigma_{rel}^x \begin{pmatrix} \widehat{\chi}_{-\sigma_A}^\dagger(\vec{r}) \\ \widehat{\chi}_{\sigma_B}^\dagger(\vec{r}) \end{pmatrix} |0, -\sigma\rangle |0, \sigma\rangle \quad (2.3)$$

$$= \begin{pmatrix} 0 & \Sigma_{AB} \\ \Sigma_{BA} & 0 \end{pmatrix} \begin{pmatrix} \widehat{\chi}_{-\sigma_A}^\dagger(\vec{r}) \\ \widehat{\chi}_{\sigma_B}^\dagger(\vec{r}) \end{pmatrix} |0, -\sigma\rangle |0, \sigma\rangle ,$$

$$\Sigma_{AB}\widehat{\chi}_{\sigma_B}^\dagger(\vec{r}) |0, \sigma\rangle = \sum_{i=1}^{N_v N} \int d\vec{r}_i \widehat{\chi}_{\sigma_i B}^\dagger(\vec{r}) |0, \sigma\rangle \, \Delta_{AB}\langle 0, -\sigma_i|\widehat{\chi}_{-\sigma_i^A}^\dagger(\vec{r}_i)V(\vec{r}_i - \vec{r})\widehat{\chi}_{-\sigma_B}(\vec{r}_i)|0, -\sigma_{i'}\rangle, \quad (2.4)$$

$$\Sigma_{BA}\widehat{\chi}_{-\sigma_A}^\dagger(\vec{r}) |0, -\sigma\rangle = \sum_{i'=1}^{N_v N} \int d\vec{r}_{i'} \widehat{\chi}_{-\sigma_{i'}^A}^\dagger(\vec{r}) |0, -\sigma\rangle \, \Delta_{BA}\langle 0, \sigma_{i'}|\widehat{\chi}_{\sigma_{i'}^B}^\dagger(\vec{r}_{i'})V(\vec{r}_{i'} - \vec{r})\widehat{\chi}_{\sigma_A}(\vec{r}_{i'})|0, \sigma_i\rangle. \quad (2.5)$$

Here interaction (2×2)-matrices Δ_{AB} and Δ_{BA} are gauge fields (or components of a gauge field). Vector-potentials for these gauge fields are introduced by the phases α_0 and $\alpha_{\pm,k}$, $k = 1, 2, 3$ of $\pi(p_z)$-electron wave functions $\psi_{p_z}(\vec{r})$ and $\psi_{p_z, \pm\vec{\delta}_k}(\vec{r})$ attributed to a given lattice site and its three nearest neighbors (see detail in [25]), $V(\vec{r})$ is the three-dimensional (3D) Coulomb potential, summation is performed on all lattice

sites and number of electrons. The introduction of these non-abelian gauge fields was stipulated by a requirement of reality of eigenvalues of the Hamiltonian operator as gauge conditions. In this case, the operator of relativistic exchange gains an additional implicit $\vec{k}$-dependence upon momentum in the case of non-zero values of gauge fields.

3. Radiation-resistant model of graphene monolayer

Carbon nanotube is a cylinder consisting of one rolled-up graphene sheet (SWCNTs) or few concentric rolled-up graphene sheets (MWCNTs). Graphene refers to strongly correlated systems. Band structure of the pure graphene holds a Dirac touching of valent and conduction bands at a Dirac point $K(K')$ of Brillouin zone. Charge carriers for the pure graphene are electron-hole pairs only. Any Dirac fermion described by a complex wave function is a composite fermion. The composition is created by a pair of conventional Majorana and antiMajorana fermions that their wave functions are real ones. Both Dirac and Majorana fermions are particles with spin $1/2$. Coulomb screening in the strongly correlated many-body graphene system impedes electromagnetic mixing of Majorana fermions back to Dirac configuration. Statistics of Majorana fermions is non-Abelian one as the rotation on the angle 2π leads to change of their wave function phase on $\pi/4$ [26]. Particles with non-Abelian statistics are called anyons. We describe a production of electron-hole pairs of zero energy in the point $K(K')$ as an emerging of the Majorana-like and antiMajorana-like fermion excitations [27, 28].

Oppositely to the Majorana fermions, eigenfunctions of our Majorana-like model Hamiltonian are complex functions. The number of electron-hole pairs of zero energy and, accordingly the pseudoMajorana quasiparticles are infinite. The Hamiltonian of Majorane-like quasiparticles and anti-quasiparticles in graphene has Majorana mass term only, an ordinary Dirac mass is absent. Features of our graphene model are the chirality of charge carriers due to their Dirac-massless state and dichroism of graphene band structure [28]. Band structure eight-folding at small quasiparticle momenta in this graphene model displays vorticity patterns (see Fig. 2). Electron-hole pairs split up (fissions) into two right- and left-handed triplets of topological defects. Thus, the three-body left (right)-handed Majorana M_p^- and right (left)-

handled antiMajorana $\overline{\mathrm{M}}_p^+$ excitations produce electrons and holes after fusion of three particles in Majorana and antiMajorana configurations respectively. A deconfinement of Majorana quasiparticles happens at sufficiently large values of momenta. Meanwhile, a Fermi velocity tends to zero. Therefore, these Majorana-like excitations are long-lived ones.
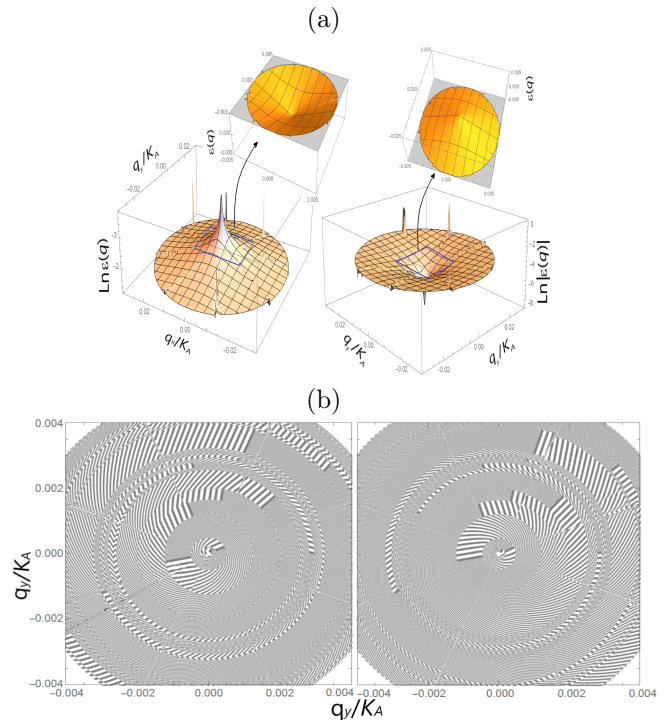

FIG. 2. (color online) (a) Electron (left) and hole (right) valent bands on momentum scale $q/K_A = 0.02$. (b) A vortex texture in contour plots of electron (left) and hole (right) bands on momentum scales $q/K_A = 0.002$. The band structure of quasi-relativistic graphene model is calculated taking into account of non-zero gauge field and Majorana-like mass term.

Elastic scattering of electromagnetic radiation quanta occurs with high probability on weakly bound electrons of conduction band [29]. Practically instant recombination of graphene electron-hole pairs in the vicinity the $K(K')$-point suppresses the Compton effect on electrons and holes in Dirac massless model of graphene.

The Majorana fermion can be presented as a chain of electrons, two of which on the ends of the

chain are delocalized, while all others electrons are in dimer configurations [30]. Therefore, such topological defects originate Comptom effect of photons scattering on delocalized charge carriers. In spite of gamma-rays the negative charged beta-particles interact with both Majorana quasiparticles and localized electrons. Elastically scattering on topological defects – Majorana quasiparticles in the Dirac point, γ- and β-quanta produce flows of deconfined Majorana configurations M_p^- and $\overline{M}_p^+$. Chirality and topological-charge conservation laws prohibit recombination of Majorana particles with charge carriers of other pairs and prevent the charge carriers from escaping outside of graphene plane. The $\overline{M}_p^+$ state is bound to a neutral knocked-out carbon atom C^0 and a neutral graphene vacancy V_g^0 appears in a non-filled lattice site. Fig. 3a schematically images the radiation damage of graphene monolayer. The vacancy V_g^0 hosts holes which emerge after fusion Majorana quasiparticles. The charged V_g^+ attracts the light M_p^-. Now, despite the fact that the heavy $\overline{M}_p^+$ with C^0 moves slowly, M_p^- await $\overline{M}_p^+$ in the non-occupied lattice site and after their fusion the knocked-out atom recovers its lattice location with subsequent repairing of graphene structure (see Fig. 3b). It testifies radiation resistivity of graphene.

charge far transfer from neutral support vacancies to positively charged areas of surface wave that a p-doped graphene patch emerges (see Fig. 3c). Pairing the charged vacancy support state $V_{\uparrow(\downarrow)}^{q+}$ and holes $h_{\downarrow(\uparrow)}^+$ holding opposite-directed spin "up" ("down") and "down" ("up") respectively are produced n-doped graphene patches (see Fig.3d). Then the heavy Majorana state $\overline{M}_p^+$ is confined in the p-doped graphene, the light state M_p^- remains in the n-doped graphene patch. As a result, n-p-n graphene junctions are formed. Escaping from plane into graphene-monolayer surface the deconfined Majorana fermions are scattered on impurities if the last exist. Transfering to low-lying orbitals of impurity, the Majorana particles quench a fluorescence of low-lying energy impurity levels because a Pauli principle forbids occupation of the same level by two identical fermions simultaneously. But, the Majorana excitations do not be able to quench a charge far transfer because their disappearing from graphene monolayer is forbidden by the law of topological-charge conservation. Therefore, the p-n graphene junctions are stable.

Further, experimental data which can be explained based on the proposed model of an artificial atom will be presented. The experimental facts will be interpreted based on the proposed model of radiation effects in graphene composite also.

4.   Formation of radiation-induced p-n graphene junction: Model

The mechanism of p-n junction formation is schematically presented in Fig. 3c,d. Laser-radiation scattering in graphene plane or scattering of photons which the knocked-out carbon atom should emit to transit in non-occupied graphene lattice site is accompanied by transmission of energy, large enough to deconfine Majorana configurations. The electromagnetic high-frequency radiation, penetrating into higher support layers, create a surface charge wave in support (skin effect). Moreover, the laser pulse or the photons emitted knocked-out atom excite a

5.   Raman-spectral analysis

Carbon nanotubes do not fluoresce. In virtue of zero energy of an electron-hole pair, if charge carriers do nor redistribute into electron and hole conduction bands from the Dirac point, than uncompensated electron/hole density in $K(K')$ is absent and, accordingly, $K(K')$ of pure graphene monolayer is electrically neutral one. Because of this, Raman scattering of light on graphene charge carriers is absent for defectless graphene monolayers.

Vibrational spectra of carbon nucleus in the electronic terms of non-compensate charge
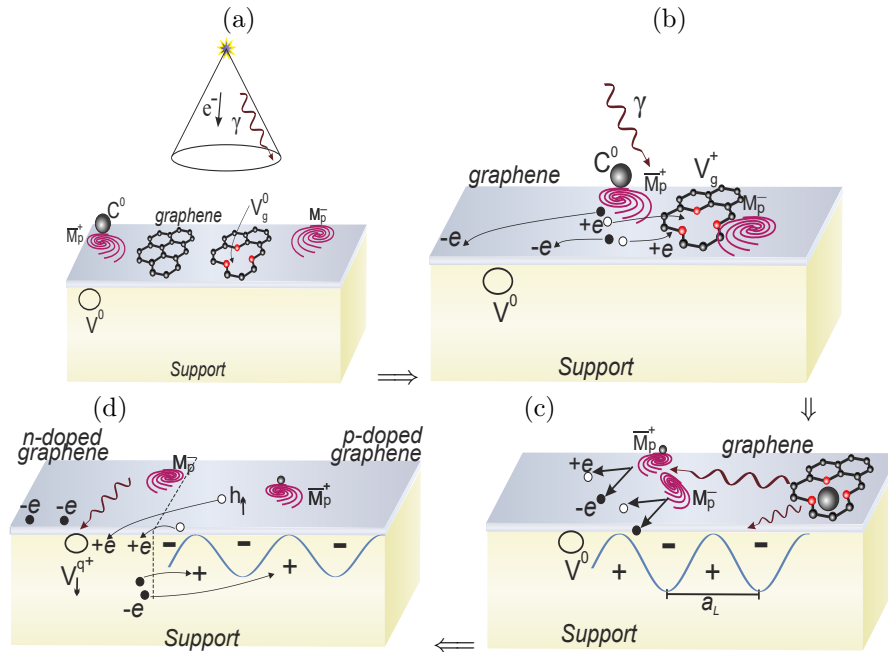
FIG. 3. (color online) A sketch of n-p-n graphene-junction formation induced by radiation. A period of charge support-surface wave is marked by a_L.

density reveal themselves in the form of the so-called defect (D) and hybridization (G) graphene bands and some other ($2D$, $2G$ etc.) of Raman spectra. The Raman scattering of light for p(n)-doped graphene monolayer occurs on charge density being in the point $K(K')$ and the point Γ of Brillouin zone. The most intensive spectral bands are the defect D and hybridized G peaks. Meanwhile carbon nuclei vibrate in the terms of gapless and gapped $\pi(p_z)$-electrons. The existence of the defect D vibration peak in the term of gapless $\pi(p_z)$-electrons evidences the possibility of electron or hole escape from graphene electron-hole pairs to impurity levels if they are presented. The Dirac point losses its electrical neutrality because of remaining free electric charge carriers of opposite sign and the Fermi level of doped graphene monolayer places higher or lower than the Dirac cone point.

The hybridization peak G testifies C nuclei vibrations in the terms of gapped $\pi(p_z)$-electrons. A value of $\pi(p_z)$-electron momentum determines a degree of mixing between $\pi(p_z)$-orbitals and

orbitals of hybridized sp-electrons. When adding sp-electrons increase the charge density in the Dirac point and, accordingly, the term of gapped $\pi(p_z)$-electron is deeper than for gapless $\pi(p_z)$-electron. It signifies that $\nu_D < \nu_G$. Table 1 displays features of Raman spectra of MWCNT-samples under investigation. Decorated or non-decorated MWCNT arrays ordered in different ways are deposited on different support.

5.1. Intensity of graphene D and G Raman bands and confinement of charge carriers to graphene plane

Let us study a transfer of MWCNT charge carriers to extrinsic impurity levels. An ensemble of original MWCNTs most intensively scatters a light in the Raman spectral bands D and G with maximums at frequencies 1328 and 1566 cm^{-1}. It signifies that the charge density in the point $K(K')$ is not compensated. A Van der Waals attractive forces between hydrophilic carboxyl residues of stearic acid and MWCNTs

Table 1. Raman characteristic frequencies ν_D, ν_G and band-intensity maxima I_D, I_G for graphene monolayers of origin multiwalled carbon nanotubes and their different bundles deposited on different support at different wavelengths λ at RT.

Support	Sample	ν_D, cm^{-1}	ν_G, cm^{-1}	I_D/I_G	λ, nm
Si hydrophilized	origin MWCNTs	1328	1566	1.165	532
	micellar MWCNTs	-*	1575	0	
	micellar oligonucleotide-encased MWCNTs	1340	1572	1.02	
	oligonucleotide-encased MWCNT one-monolayer film			0.81	
	three-monolayer non-decorated MWCNT LB-film	1400–1403	1586	0.25	355
	two-monolayer organometallic-compound-decorated MWCNT LB-film	-	-	-	532
		1398–1400	1597–1600	0.1875	473
AOA hydrophilized		-	-	-	532
	two-monolayer non-decorated MWCNT LB-film	1353	1573	0.75	473
AOA hydrophobized				0.167	

* – Hyphen means that a corresponding peak is absent.

form inverse micelles of stearic acids, hydrophobic alkyl hydrocarbon chain of which are directed outside. Meanwhile, MWCNTs are placed inside the micelles. Micellar MWCNTs were deposited on hydrophobized or hydrophilized surface of AOA and hydrophilized Si. Since the peak D disappears practically for samples of micellar MWCNTs, electric charge carriers are absent in the Dirac point and the Fermi level is in the Dirac band touching. It signifies that micellar MWCNTs inside inverse micelles are self-organized into a high-ordered ensemble with practically defectless structure. According to Table 1, the peak D appears again in the spectra of LB-films formed from inverse micelles with nondecorated MWCNTs inside after their deposition on the support. Repulsion between hydrophobic groups of LB-film and hydrophilic groups of the support leads to emerging of graphene-lattice deformation defects. Localization of charge carriers from MWCNTs electron-hole pairs on such impurity levels originates non-compensated charge density

in $K(K')$ and Γ. Meanwhile, the Fermi level shifts from the touching point of graphene electron and hole conduction bands. Owing to the law of spirality conservation, the free charge carriers do not annihilate with other remaining charge carriers of opposite sign. Because the number of Majorana particles is infinite large, the electric charge transfer happens to impurity levels of all defects. The charge carriers in graphene materials do not recombine with impurity and support-defect states owing to the law of topological-charge conservation. As Table 1 demonstrates, the height of peak D increases at rise of the number of impurity levels, electron (hole) density of which forms bound states (excitons) with graphene charge carriers. A quantity of states bound to impurity levels is determined by electrocapillary effects (electrocapillary forces). The hydrophobic LB-MWCNT-film extends on hydrophobic surface under the action of electrocapillary forces uniformly. Meanwhile CNTs straighten up moving

away the support. On the hydrophilic surface the action of electrocapillary forces bending the hyrdophobic film leads to emerging of regions where CNTs abut on the support very closely. Because of this the intensity ratio I_D/I_G for the peaks D and G of scattering in the hydrophobic LB-film with two non-decorated-MWCNT monolayers is significant less in the case of hydrophobic AOA support ($I_D/I_G = 0.167$), than in the case of hydrophilic AOA support ($I_D/I_G = 0.167$, see Table 1). Similarly, micellar MWCNTs which do not touch the support surface, have not the defect levels and, accordingly, the peak D is absent in their spectra. Oppositely, due to a strong contact between individual bend original MWCNTs and Si support the ratio takes a high value: $I_D/I_G = 1.165$.

So, the graphene charge carriers are held in the vicinity of the MWCNT-surface. This confinement phenomenon occurs due to fact that electrons and holes are produced in Majorana and antiMajorana configurations. When flatting the energy band prevents the fusion of Majorana and antiMajorana quasiparticle due to zero Fermi velocity: $v_F \to 0$ at high momenta. At that, the infinitely large Majorana force confines the graphene charge carriers inducing transitions of the charge carriers from high-lying levels to low-lying ones [33]. The latter precludes pairing between the graphene charge carriers and the opposite-charged impurity electrons (holes) on the high-lying impurity levels.

The frequencies ν_D and ν_G of characteristic vibrations do not depend on the height of D- and G-peaks and, accordingly, do not depend on the number of graphene charge carriers localized on the impurity levels of a given type. For example, according to Table 1, $\nu_D = 1353$ nm and $\nu_G = 1573$ nm at laser excitation 473 nm for MWCNTs which are arranged on both hydrophilized and hydrophobized AOA surfaces. Another example, $\nu_D = 1340$ nm and $\nu_G = 1572$ nm at laser excitation 532 nm for micellar oligonucleotide-encased MWCNTs and the LB-monolayer consisting of oligonucleotide-encased MWCNTs (see Table 1). D- and G-bands position for

MWCNTs at given laser wavelength and at the same type of the impurity level indicates that the graphene lattice-deformation defects linked to the Dirac point and, accordingly, do not take external charge carriers on their energy levels.

5.2. Quenching effect

The oligonucleotide cover of MWCNTs does not fluoresce because the Majorana quasiparticles occupy oligonucleotide low-lying levels. Thus, the scattering of electromagnetic radiation in aromatic compounds deposited on graphene surface is quenched. The charge carriers of graphene material do not quench high-lying levels of support defects because the Majorana particles can be just in graphene plane. One observes sharp decrease of I_D/I_G at $\lambda_{ex} = 355$ nm in comparison with the excitation $\lambda_{ex} = 473, 532$ nm for the defective support and samples (see Table 1). It testifies also that the pseudo-Majorana states transfer from the impurity back to the graphene monolayer because they are not able to hybridize with high-lying impurity orbitals.

5.3. Emerging graphene D, G bands at support-defect charging

An electromagnetic field penetrates into a sample to a definite depth (skin effect). The penetration depth of a electromagnetic field is about a half of the wavelength. Penetrating into a sample, the electromagnetic quanta excite surface states. A superstructure of graphene monolayer is induced due to the skin effect. Let us prove that electrical fields of charged support vacancies destroy the graphene supercells, and remaining supercells represent artificial atoms. To make it we study Raman spectra of the high-ordered LB-monolayers which consist of MWCNTs decorated by the organometallic complexes and are arranged on Si or nanoporous anodic alumina.

The value ν_D depends on laser wavelength values λ_{ex} so that ν_D increases with decrease of λ_{ex} as Table 1 demonstrates. At the average it grows also with the decrease of λ_{ex} (see

Table 1). The Raman frequencies are higher if the band structure of MWCNT-samples is distorted less. For example, at the same laser wavelength λ_{ex} =532 nm ν_G = 1566 and 1575 cm^{-1} for chaotic arranged origin and micellar MWCNTs respectively. The highest charge density in the Dirac point is achieved in the LB-films of decorated MWCNTs as ν_G = 1587 − 1600 nm at λ_{ex} = 473 nm and ν_G =1586 cm^{-1} at λ_{ex} = 355 nm for the decorated MWCNTs and the LB-film of non-decorated MWCNTs respectively on Si support.

Thus, our model predicts and the experimental data testify that variation of p-doping conditions stems from the variation of superlattice potential. The frequencies ν_D and ν_G depend on λ_{ex} because the parameters of surface wave determine the graphene supercells.

5.4. CNT-enhanced scattering light in metal-containing DTP LB-films

The peaks D and G are not observed for decorated MWCNTs suspended на AOA nanopores at λ_{ex} = 473, 532 nm and for MWCNTs deposited on Si at λ_{ex} = 532 nm. The absence of characteristic bands of MWCNTs in Raman spectra testifies the practically perfect crystal structure of decorated-MWCNT-monolayers with neutral Dirac point (see Table 1). The charge carriers do not be transferred along the LB-DTP-film at laser excitation with wavelength 473 nm but accumulate in sites of contact between molecules Fe(II)DTP and Si surface because of disruption of double-bound chain with the subsequent localization of charge carriers. The value of I_D/I_G equals to 0.1875 at λ_{ex} =473 nm and is comparable with I_D/I_G = 0.25 at λ_{ex} =355 nm for decorated and non-decorated MWCNTs respectively that indicates the long charge transport to high-lying levels where graphene charge carriers are not able to exist. The graphene charge carriers holding in the electric field of charged high-energy surface states form the artificial atoms. Since a MWCNT-plasmon enhancement of light scattering for the

DTP LB-film on Si at 473 nm disappears, practically all free charge carriers enter the artificial atoms. On the contrary, the Raman spectra for the decorated MWCNTs suspended on AOA nanopores do not distinguished at laser excitations with wavelengths 473 and 532 nm due to the absence of support and, accordingly, of charged support defects.

Different-type MWCNT arrays shield electric fields with different efficiency. The quantity of charged support vacancies is much less at more effective screening. Therefore, the artificial atoms and the potential electrically confining these p-doped graphene patches are much bigger at the effective screening of support. Nuclei C oscillate much faster for the deep confining potential than shallow one. For example, accordingly to Table 1, the values of ν_D and ν_G are larger for the MWCNT array decorated by organometallic-compound than oligonucleotide-encased one because the former shields better than the later.

6. Impedance analysis

Dielectric spectra of non-exposed structures under investigation are presented in Fig. 4. Unlike to the graphene-like materials the dielectric spectra of AOA do not have specific dielectric Cole-Cole plots with a diffuse element or Warburg impedance W. Since the Warburg impedance is absent for AOA and, consequently, aluminium-electrodes oxidation does not happen, the fabricated nanoheterostructures are stable. The Cole-Cole plot for metal-containing dithionylpyrrole LB-films testifies both the Warburg impedance element W of diffuse layer in which the electrochemical reactions with mass transfer proceed and an electric capacity of Helmholtz double layer. For the dithionylpyrrole LB-films, this oxidation-reduction potential stipulated by change of molecular-group charge state arises due to self-redox activity of pyrrole residue and transport of electrical charge along the chain of conjugated double bonds. MWCNTs, as LB-DTP-films, are redox active themself

according to the Cole-Cole plot of spectrum 3 with W in Fig. 4. The change of charge state of K(K') point is associated with mass transfer that Kitaev-like chains with Majorana end states emerge. Meanwhile, plasma oscillations of produced electron-hole pairs shield electric field of charged electrodes.

According to Bode capacity plots 1, 2, and 4 in Fig. 5a for irradiated and non-irradiated organometallic-compound LB-films a dipole relaxation of radiation-vacancies clusters is observed simultaneously with the increase of shielding degree in two weeks after irradiation by IRS ^{137}Ce. The sharp increase of shielding degree indicates that the number of free charge carriers increase extremely. Because electron-hole pairs are charge carriers in graphene and graphene-like materials, the increase of free charge carriers density indicates localization of holes or electrons from electron-hole pairs after irradiation. The incoming particles can collide with electrons only. Since the atoms C are knocked out, holes (vacancies) localized in the Dirac point remain.

The charge density of vacancies ensemble has a form of atom-like density of localized holes surrounded by delocalized electron density. The dipole relaxation of these individual radiation-vacancy ensembles disappears for long enough time about three months according to comparison of dielectric spectra 2 and 3 in Fig. 5a. Emerging only two weeks latter after irradiation the individual atom-like vacancy arrays indicate a decay of very large cluster of radiation vacancies into the small atom-like arrays (artificial atoms) in graphene-like monolayer plane during self-repairing processes.

Because the high energy of gamma- and beta-rays produced by IRS the atom-like ensembles of radiation vacancies are produced in excited state with non-occupied both valence and intrinsic orbitals by the mechanism proposed in Section 4. Overlapping the external orbitals of such artificial atoms in excited state produce large radiation-clusters of vacancies. Hydrate complexes of atom-like structures formed by vacancies are produced after transition of the last into the ground state after two weeks according
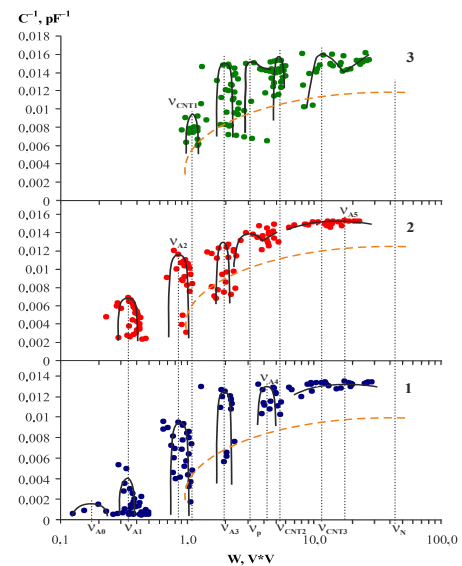

FIG. 4. (color online) Dielectric spectra 1 for nanoporous AOA, 2 and 3 for наногетероструктур based on Ce-containing nanocyclic compound Fe(II)DTP and on decorated MWCNTs, respectively. Resonance frequencies ν of Cole-Cole plots in the spectra are marked as $\nu_{Ai}, i = 0, \dots, 5$ for AOA; ν_P for the organometallic compound and $\nu_{CNTi}, i = 1, 2, 3$ for MWCNTs. A Nyquist plot of impedance for the measuring circuit is marked by a yellow dashed line with ν_N.

the comparison of the Bode plots 1 and 2, Fig. 5a. This is evidence that the external orbitals in the ground state is not overlapped. The decay of large radiation cluster into the separated artificial atoms (electrically confined quantum dots) is testified by the corresponding resonance at the frequency ~ 280 kHz for the metal-containing LB-film. A lifetime of individual quantum dot is very large so that the dots exist for one–two months.

Mobile interstitial carbon atoms being near monolayer plane can form chemical cross-links with hydrocarbon alkyl chains. According to comparison of the frequency dependencies 3 and 4 in Fig. 5a, after decay of artificial atoms the variation of electrophysical properties of metal-containing dithionylpyrrole LB-films is reduced practically to a weak increase of original value of the sensor electric capacity. The weak increase is
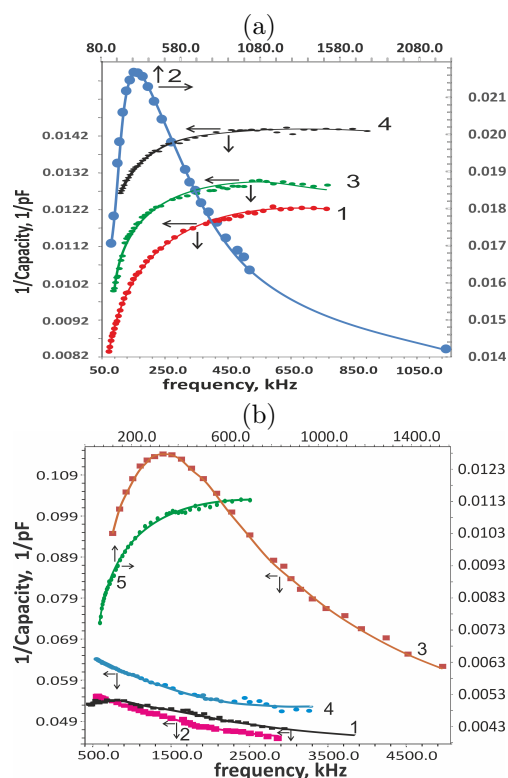
FIG. 5. (color online) Frequency dependences of electrical capacity: (a) of Fe-containing dithionylpyrrole LB-film and (b) MWCNTs decorated by nanocyclic complexes of Fe and Ce with dithionylpyrrole ligands. (a) 1 - immediately after irradiation, 2 - in two weeks after irradiation, 3 - in three months after irradiation, 4 - before irradiation; the duration of irradiation was 1 hour. (b) 1 - immediately after irradiation, 2 - in 24 hours after irradiation, 3 - in three weeks after irradiation, 4 - in four months after irradiation, 5 - before irradiation; the duration of irradiation was 3 hours.

stipulated by a small destroying of the double-bound chains by the cross-links with near-lying alkyl hydrocarbon chains and, respectively, by an attenuation of shielding effect .

A mechanism of MWCNT radiation resistivity is similar to the mechanism for metal-containing dithionylpyrrole LB-film. The dielectric spectra of irradiated LB-films of MWCNTs decorated by nanocyclic complexes of Ce and octahedral high-spin Fe, are presented in Fig. 5b. According to the Bode plot 3,

Fig. 5b, the dipole relaxation of hydrated atom-like clusters of radiation vacancies occurs at higher frequencies (about 1320 kHz) than in the dithionylpyrrole films. This is due to the restriction of the artificial atom size by CNT diameter value. According to the Bode plots 1–4, Fig. 5b, the decay of excited radiation-induced artificial-atom aggregates occurs in three weeks after irradiation, while the restoration of electrophysical properties of MWCNTs occurs in three month after the irradiation when quasi-stationary artificial atoms disappear. The shift of the maximum in the frequency dependence 1, Fig. 5b towards low frequencies is registered immediately after irradiation also. This shift indicates the formation of atom-like clusters of the vacancies under the action of γ- and β-rays in the metal-containing dithionylpyrrole LB-monolayers decorating MWCNTs.

Decrease of electric capacity of non-irradiated MWCNTs from 85.2 pF to 18.5 pF is registered immediately after three-hour irradiation. Accordingly, the increase of the intensity in the Bode plot 1 in respect of the plot 5 in Fig. 5b testifies the high shielding efficiency of MWCNTs-network and, accordingly, its high electric conductivity. It signifies that in the addition to the radiation-resistivity mechanism for metal-containing dithionylpyrrole LB-film there is cross-connections between graphene monolayers of MWCNT and interstital knocked-out atoms C through chemical bounds into a high-shielding network.

Shielding effects of the LB-films is revealed also as an intensity change of Compton scattering and as an increase of intensity of secondary electrons spectra in the detector of γ-rays.

Thus, as the quasi-relativistic graphene model predicts, the experimental study fulfilled discovers that there exists a Compton effect at irradiation of the graphene-like material. Further, we propose a model of the Compton effect enhanced by a collapse of artificial heavy atomic states in graphene monolayers.

7. Enhancement of Compton effect in graphene

Accordingly to the experimental data, a time of dipole relaxation is about 0.7 μs. Such large relaxation times testify that the p-n junctions are sufficiently big. The relaxation process is observed only after a time τ_C about 2–3 weeks after irradiation. Therefore, τ_C is time for which the cluster of original artificial atoms decays. It signifies that the original artificial atoms are chemically linked in the cluster with a life time τ_C. A life time τ_J of free artificial atoms appearing after decay of the large radiation cluster is much longer, more than a month. After this period the electrochemical properties of the samples are recovered. Since the orbitals of original artificial atoms overlap, they are much larger than for the free p-n junctions. But, large atoms with ultra-heavy nuclei are in a supercritical regime that is the electronic orbitals, starting with 1S state, sink into the Dirac continuum until an atom number Z is reduced to a critical value. This process is known as atomic collapse [34]. Opposite to the supercriticality of an atom, the orbitals of artificial atom sink into the Majorana continuum until Z is reduced to a critical value. An enormous number of secondary delocalized electrons emerging after fusion between sunken M_p^-–vortices and $\overline{M}_p^+$–anti-vortices provides sharp increase of the photon elastic scattering cross-section. The very large electron density in the irradiated samples is registered by scintillator as significant bend of direction of propagation of γ-quanta from the original once. After the atom-state collapses the hybridized charge carriers are on high-lying discrete energy levels of p-n graphene junction. Such cluster is unstable due to its high energy accordingly to the electrochemical study.

8. Discussion and conclusion

Let us estimate the performance of graphene composites under investigation as radiation detectors. Since very much low-energy electron-hole pairs are produced in graphene monolayer after the scattering of electromagnetic quanta on the topological defects, the scattering cross-section S_M^f on the topological defects is much smaller than a scattering cross-section S_{e-h}^f of free electron-hole pairs:

$$k_{Mf} = S_{e-h}^f/S_M^f \gg 1. \qquad (8.1)$$

Let us call the value k_{Mf} as an enhancement coefficient due to production of free electron-hole pairs. Sub-picosecond recombination of electrons and holes attenuates this enhancement so that $k_{Mf} > 1$. However, the cross-section of the elastic scattering of photons on the secondary delocalized electrons from the artificial collapsed atom is a significant effect. Let us suppose that the cross-section of Comptom scattering on the secondary electrons is larger than the cross-section of the scattering on the electrons from electron-hole pairs by R_A^2/R_{e-h}^2. Here R_{e-h} is a radius of free electron-hole pair of about an atom size, R_A is a radius of nanosize artificial atom. Besides, photons emitted by knocked C^0 during its occupation of free lattice site form the atom-like structures in the nearest monolayers also. Because of that, the final enhancement coefficient k_γ of Compton scattering is also proportional to a number of graphene monolayers N_w:

$$k_\gamma = k_{Mf} N_w R_A^2/R_{e-h}^2 \gg 1. \qquad (8.2)$$

Substituting (8.1) into (8.2), one get

$$k_\gamma = N_w S_A/S_M^f \gg 1 \qquad (8.3)$$

as $S_{e-h}^f \sim R_{e-h}^2$. Here S_A is a scattering cross-section of artificial atom. In the case of LB-films contained from MWCNTs, it is necessary to take into account the MWCNT-layer number. This shielding of radiation defect by avalanche-like increase of the number of free charge carriers comes to minimum the radiation destruction of graphene-like material.

Beta-particle detection. Opposite to gamma-rays detection, Coulomb interaction of negative-charged beta-particle occurs not only with free Majorana particles, but also with bound electron-hole pairs. Therefore, the enhancement coefficient

of scattering by graphene plane due to collisions with Majorana quasiparticles is

$$k_M = k_{Mf} + k_{Mb} = k_{Mf} + S^b_{e-h}/S^b_M \gg 1 \quad (8.4)$$

where S^b_M and S^b_{e-h} are the cross-sections for the scattering on the bound Majorana states and on the bound electron-hole pairs, respectively. Although $S^b_{e-h}/S^b_M \gg 1$, because of the subpicosecond electron-hole recombination the ratio k_M is not much higher than k^f_M. Further enhancement of β-scattering occurs by avalanche-like increase of charge carriers number by the mechanism similarly as for γ-rays. Besides, β^--particles can additionally interact with enormous number electrons localized in n-doped graphene patch. Therefore, assuming that $S^b_{e-h} \approx S^f_{e-h}$, the enhancement coefficient k_β of Coulomb scattering of β-particles on N_w graphene planes is determined by the following expression:

$$k_\beta = k_M N_w R^2_A/R^2_{e-h} + k_{nd}$$
$$= N_w S_A \left(\frac{1}{S^f_M} + \frac{1}{S^b_M} \right) + k_{nd} \gg 1 \quad (8.5)$$

where k_{nd} is the enhancement coefficient of the elastic β-scattering due to the existence of n-doped graphene patch.

So, the defects created under the action of 650 keV gamma- and 1 MeV beta-radiation do not lead to radiation destruction both two-monolayer LB-films of MWCNTs decorated by nanocyclic organometallic complexes and the ultra-thin metal-containing conductive oligomer LB-films. Collisions of bombarding particles with delocalized electron density of the topological defects in graphene material form the flows of electron-hole pairs. Radiation resistance of synthesized graphene-like materials is provided by stabilization of the band structure due to confinement of the hole part of electron-hole pairs density in of $K(K')$-point charged due to electron/holes fluxes from the topological defects. At that, the radiation clusters consisting of nanosize artificial atoms (n-p-n junctions) are created in the graphene monolayer. The sink of charge carriers into the Majorana continuum with a collapse of atomic states occurs. The cross-section of elastic scattering of γ-quanta grows effectively due to existence of these secondary electrons. The overlap of high-lying orbitals of p-n junctions produces quasi-stable "crystal" (cluster) of the artificial atoms. Dipole relaxation for the artificial crystal provided by the displacement of its artificial atoms happens at high frequencies. When the crystal decays, the reorientation of dipole moments of the individual artificial atoms takes place at low frequencies.

References

[1] Y.-f. Xiong *et al.* Ultrahigh Responsivity Photodetectors of Two-dimensional Covalent Organic Frameworks Integrated on Graphene. Advanced Materials. **32**, 1907242 (2020).

[2] V.L. Gurachevski. *Radiation control : Physical foundation and instrumental equipment.* (Radiology Institute Press, Minsk, 2014). (in Russian)

[3] J. Lindhard. Influence of crystal lattice on motion of energetic charged particles. Matematisk-Fysiske Meddelelser Det Kongelige Danske Videnskabernes Selskab. **34**, 1-65 (1965).

[4] H. Huang *et al.* Graphene damage effects on radiation-resistance and configuration of copper-graphene nanocomposite under irradiation: A molecular dynamics study. Scientific Reports. **6**, 39391 (2016).

[5] Y. Kim *et al.* Radiation resistant vanadium-graphene nanolayered composite. Sci. Rep. **6**, 24785 (2016).

[6] L.S. Novikov, E.N. Voronina. *Prospect of nanomaterials applying in cosmic technics.* (University book, Moscow, 2008). (in Russian)

[7] G. Chai, H. Heinrich, L. Chow, T. Schenkel. Appl. Phys. Lett. **91**, 103101 (2007).

[8] M.C. Evora *et al.* Effect of electron beam and

gamma rays on carbon nanotube yarn structure. Materials Research. **20**(Suppl. 2), 386(2017).

[9] S.N. Shul'ga *et al.* On classical and quantum effects at scattering of ultrarelativistic electrons in ultrathin crystal. Nucl. Instrum. Methods Phys. Res. Sect. B. **402**, 16(2017).

[10] Y. Takabayashi, Y.L. Pivovarov, T.A. Tukhfatullin. First observation of scattering of sub-GeV electrons in ultrathin Si crystal at planar alignment and its relevance to crystal-assisted 1D rainbow scattering. Phys. Lett. B. **785**, 347 (2018).

[11] M. Ćosić, S. Petrovi, N. Nešković. Quantum rainbows in positron transmission through Carbon Nanotubes. Atoms. Vol. 7, 16 (2019).

[12] B. Li *et al.* The effect of gamma ray irradiation on the structure of graphite and multiwalled carbon nanotubes. Carbon. **60**, 186 (2013).

[13] J. Mao *et al.* Realization of a tunable artificial atom at a supercritical charged vacancy in graphene. Nature Phys. **12**, 545 (2016).

[14] A.V. Korol, A.V. Solov'yov, W. Greiner. *Channeling and Radiation in Periodically Bent Crystals.* (Springer-Verlag, Berlin, Heidelberg, 2014).

[15] V.V. Klimov, V.S. Letokhov. Monochromatic γ-radiation emitted by a relativistic electron moving in a carbon nanotube. Phys. Lett. A. **226**, 244 (1997).

[16] X. Artru *et al.* Carbon nanotubes and fullerites in high-energy and X-ray physics. Phys. Rep. **412**, 89 (2005).

[17] C.-H. Liu *et al.* Graphene photodetectors with ultra-broadband and high responsivity at room temperature. Nat Nanotechnol. **9**(4), 273 (2014).

[18] A. Agrawal, G.H. McKinley. Nanobubble formation at the solid-liquid interface studied by atomic force microscopy. Materials Research Society Symposium Proceedings. **899**E, Paper 0899-N07-37 (2006).

[19] Nucl. Data Sheets. **108**, 2173 (2007).

[20] T.E. Konstantinova, E.I. Lyafer. Hydrostatic compaction pressure influence on sintered spodumene pyroceramics properties. In: *High pressure science and technology.* Ed. W.T. Trzeciakowski. (World Scientific Publishing, Singapore, 1996). Pp. 118-120.

[21] I.I. Abramov *et al.* A method of impedance calculation for impedimetric sensor with interdigital structure Petersburg electronics J.

[22] H.V. Grushevskaya, G.G. Krylov, In: *Graphene Science Handbook: Electrical and Optical Properties.* Vol. 3. Chapter 9. Eds. M. Aliofkhazraei *et al.*Taylor and Francis Group, CRC Press, USA, UK, 2016.

[23] H. Grushevskaya, G. Krylov. Vortex Dynamics of Charge Carriers in the Quasi-Relativistic Graphene Model: High-Energy $k > \cdot p >$ Approximation Symmetry **12**, 261 (2020).

[24] H.V. Grushevskaya, G. Krylov. Semimetals with Fermi Velocity Affected by Exchange Interactions: Two Dimensional Majorana Charge Carriers. J. Nonlin. Phenom. in Complex Sys. **18**, 266 (2015).

[25] H.V. Grushevskaya *et al.* Symmetry of Model N = 3 for Graphene with Charged Pseudo-Excitons. Int. J. Nonlin. Phenom. in Complex Sys. **18**, 81 (2015).

[26] C.W.J. Beenakker. Search for Majorana Fermions in Superconductors. Annu. Rev. Condens. Matt. Phys. **4**, 113-136 (2013).

[27] H.V. Grushevskaya, G.G. Krylov. Massless Majorana-like charged carriers in two-dimensional semimetals. Symmetry. **8**, 60 (2016).

[28] H.V. Grushevskaya, G.G. Krylov. Increasing Spin-Orbital Coupling at Relativistic Exchange Interaction of Electron-Hole Pairs in Graphene. Semiconductors. **52**, 1879 (2018).

[29] E.A. Murzina. *Interaction of radiation with matter.* (KDU, Moscow, 2007). (in Russian)

[30] A.Y. Kitaev. Unpaired Majorana fermions in quantum wires. Physics Uspekhi. **44** (Suppl.), 131 (2001).

[31] Ch. Gutierrez *et al.* Klein tunnelling and electron trapping in nanometre-scale graphene quantum dots. Nature Physics. **12**, 1069 (2016).

[32] V.A. Starodubtsev, T.V. Fursa, N.N. Zausaeva. Charge electrification of irradiated dielectrics and its effect on incident flux. J. Electrostatics. **20**, 341 (1988).

[33] H.V. Grushevskaya, G. Krylov. Two-Dimensional braiding of two-dimensional majorana fermions : manifestation in band structure of graphene. Int. J. Nonlinear Phenom. Compl. Systems. **22**, 41 (2019).

[34] Y.B. Zel'dovich, V.S. Popov. Electronic structure of superheavy atoms // Sov. Phys. Usp. Vol. 14, 673-694 (1972).